Growth of Epitaxial Oxide Thin Films on Graphene

Bin Zou[1], Clementine Walker[1], Kai Wang[1], Vasiliki Tileli[1], Olena Shaforost[1], Nicholas M. Harrison[2], Norbert Klein[1], Neil M. Alford[1] and Peter K. Petrov[1*]

[1] Department of Materials, Imperial College London, Prince Consort Road, London, SW7 2AZ, UK

[2] Department of Chemistry, Imperial College London, Imperial College Road, London, SW7 2AZ, UK

*e-mail: p.petrov@imperial.ac.uk

Abstract

The transfer process of graphene onto the surface of oxide substrates is well known. However, for many devices, we require high quality oxide thin films on the surface of graphene. This step is not understood. It is not clear why the oxide should adopt the epitaxy of the underlying oxide layer when it is deposited on graphene where there is no lattice match. To date there has been no explanation or suggestion of mechanisms which clarify this step. Here we show a mechanism, supported by first principles simulation and structural characterisation results, for the growth of oxide thin films on graphene. We describe the growth of epitaxial $SrTiO_3$ (STO) thin films on a graphene and show that local defects in the graphene layer (e.g. grain boundaries) act as bridge-pillar spots that enable the epitaxial growth of STO thin films on the surface of the graphene layer. This study, and in particular the suggestion of a mechanism for epitaxial growth of oxides on graphene, offers new directions to exploit the development of oxide/graphene multilayer structures and devices.

Main text

Graphene has attracted great interest because of its outstanding electronic[1,2,3,4], optical and physical properties.[1,5,6,7] It exhibits extraordinarily high electronic quality which is usually characterized by mobility of its charge carriers. Monocrystalline graphitic films (a few atoms thick) exhibit electron and hole concentrations up to $10^{13}cm^{-2}$ with charge mobility of ~10,000 cm^2/Vs at room temperature (RT).[1] The charge carriers in such thin graphitic films are confined to two dimensions. Graphene,

a 2D sheet of carbon atoms, is very stable at room temperature and in air, where it maintains macroscopic continuity and its carrier mobility remains almost unaffected.[8] High electrical conductivity of 1738 $S \cdot m^{-1}$ has been obtained in graphene produced by direct laser reduction.[9] In addition to the extraordinary optical and electrical properties, graphene has excellent mechanical properties which mean that it can be used extensively as a flexible and stretchable electrode.[6] These unusual characteristics of graphene suggests its use as electrodes[10] (thin, conductive, elastic and stiff) and for many electronic devices, such as transistors[11], solar cells[12,13], capacitors[14] and microwave acoustic resonators[15,16,17].

The development of technology for fabrication of oxide on graphene structures is essential for the realization of industry-attractive graphene based devices. Therefore, it is necessary to develop a method for deposition of atomically uniform oxide layers without damaging the underlying graphene and without creating high interface defect density between the graphene and oxide materials.[18] Although Al_2O_3, HfO_2 and SiO_2, have been successfully deposited on graphene via atomic layer deposition (ALD), pulsed laser deposition (PLD), sputtering and e-beam evaporation,[18,19,20,21] its growth mechanism is still unclear.

Herein, we propose a growth mechanism that explains the formation of epitaxial $SrTiO_3$ (STO) thin films on graphene, which were prepared by chemical vapour deposition (CVD) and subsequently transferred onto STO and MgO substrates. The

suggested mechanism is supported by density functional theory (DFT) modelling and verified by structural and electrical characterisations.

The graphene/$SrTiO_3$ (Gr/STO) interface was modelled in a 2D-periodic square cell of side 8.85 Å containing 10 STO formula units representing four atomic layers of the (100) surface in a $\begin{pmatrix} 2 & 1 \\ -1 & 2 \end{pmatrix}$ supercell of the primitive surface unit cell and 60 carbon atoms representing graphene sheets at both the SrO and TiO_2 terminations in a $\begin{pmatrix} 1 & 4 \\ 4 & 1 \end{pmatrix}$ supercell of the primitive graphene unit cell. This is the smallest near commensurate (strain < 2.5%) periodic representation of the Gr/STO (100) interface (Fig. 1). In the optimised geometry the plane of the graphene sheets sit 3.19 Å above the Sr ions of the surface SrO layer and 3.08 Å above the Ti ions of the TiO_2 surface layer. The average binding energy of the graphene to the oxide surfaces is 56 meV per C-atom. Calculation of the electrostatic field above the sheet establishes that the corrugation in the electrostatic potential is negligible suggesting that a complete graphene sheet will screen oxide overlayers from the direct influence of the substrate. This is confirmed by an explicit calculation of the corrugation potential computed by adding a periodic SrO sheet above the graphene layer and computing its energy on a 10×10 grid of points as it slides across the surface (perpendicular atomic coordinates optimised for each configuration). The resultant energy surface has a corrugation of less than 1meV per carbon atom. Undisturbed through-graphene layer epitaxial growth mediated by wrinkling of the graphene sheet or electrostatic interactions is therefore highly unlikely.

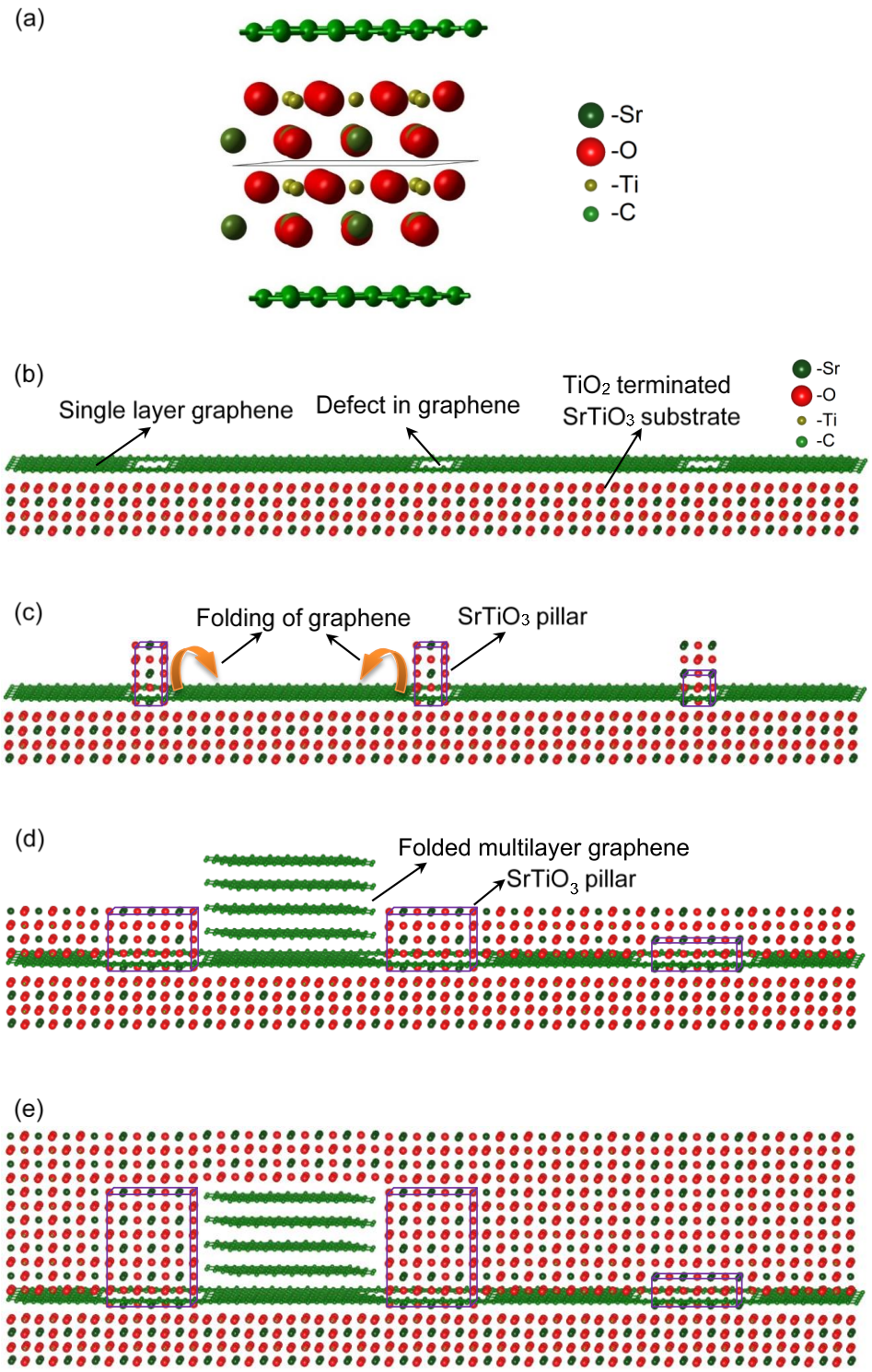

Figure 1: Growth process of oriented single crystal STO film on a graphene layer: (a) a unit cell of the optimised STO (100) surface structure with graphene adsorbed. The bonded green spheres represent C, large (red) spheres – O , medium (dark green) spheres – Sr and small spheres – Ti; (b-e) schematic diagram of the growth mechanism: (b) single graphene layer transferred onto TiO_2 terminated STO

substrate; (c) initial nucleation of the STO cells onto the STO substrate through the defects of the graphene layer; (d) in-plane growth of the oriented STO “pillars” that results in folding of the graphene layer, and formation of the over-single-graphene-layer epitaxial STO “bridge” structure (not to scale); (e) follow-up deposition of the single crystal epitaxial STO film. The crystallographic structures in (b)-(e) were visualized using VESTA.[22]

The ease with which the sheet slides across the oxide surface suggests an alternative mechanism for epitaxial growth. Defects in the sheet introduced during the graphene growth or transfer provide reaction centres for the adsorbing oxide and may allow bridge structures to form between the substrate and the oxide overlayer. In this scenario, an oriented single crystal STO film on a graphene layer might be supported by epitaxial pillars grown through the defects in the graphene layer (e.g. grain boundaries) (Fig. 1.b). Within these defects in the graphene layer, the STO layer grows epitaxially (following the substrate template) in both in-plane and out-of-plane directions. Initially, the in-plane nucleation and growth of the STO layer is obstructed by the graphene layer. The generated interfacial shear force slides and folds the graphene layer, which is weakly bonded to the substrate (Fig. 1c). Once the STO pillars grow above the graphene then the in-plane growth of the STO layer is not restrained, which allows formation of the over-single-graphene-layer epitaxial STO “bridge” structure (Fig. 1d). This could be achieved with appropriate ad-atoms saturation ratio, which is a measure of the driving force of the diffusion, of the surface reactions and of the nucleation. Hence if the flux of the incoming species and their energies are high enough to enable diffusion along the surface and nucleation before

their re-evaporation then one could have highly oriented film grown between the epitaxial pillars (Fig. 1e). This suggests that PLD should be the preferred deposition method as the species produced during the laser ablation arrive on the sample surface with relatively high energies.

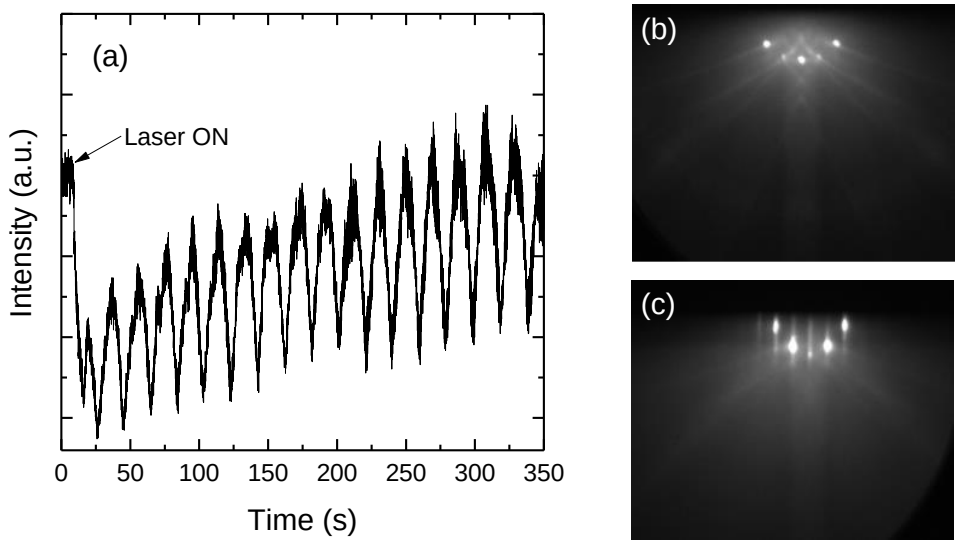

Figure 2: (a) Specular RHEED intensity recorded during initial growth of STO (only showing the initial 18 unit cell layers); (b) RHEED patterns recorded before growing STO on Gr/STO (100) at RT and (c) after growing 100nm STO/Gr/STO (100) at 850^{o}C.

In this study, 100 nm STO thin films were grown on Gr/MgO and Gr/STO by PLD at 850^{o}C in ultra-high vacuum (~10^{-8}Torr). The thin film growth was monitored using reflection high energy electron diffraction (RHEED). The specular RHEED intensity shows a sharp decrease and a recovery during deposition of the first unit cell, illustrated in Fig. 2(a). The magnitude of the oscillation increased with the number of layers grown, as did the total intensity. This is an indication of improving surface

smoothness. The growth rate of STO is 39 pulses/unit-cell derived from RHEED oscillations. The RHEED patterns of Gr/STO (100) sample and STO/Gr/STO (100) sample are depicted in Fig. 2(b) and (c), respectively. After growing the STO thin film, the very sharp 2D spots, originating from the STO substrate, were slightly blurred into streaks. The streaks and weak oscillation are indications of a roughened surface caused by the increased step density on the surface.

Fig. 3 shows X-ray diffraction (XRD) patterns of STO grown on Gr/MgO and Gr/STO. The XRD pattern of STO/Gr/STO shows exclusively STO (00*l*) peaks from 2θ of 20^{o} to 120^{o} (not fully shown here). This indicates that STO was epitaxially grown on Gr/STO. To further prove the growth of STO on graphene, STO films were deposited on Gr/MgO. The (002) STO peak clearly appeared on the XRD pattern of STO/Gr/MgO, shown in Fig. 3(a), as well as the (004) peak, shown in Fig. 3(b). The current (I)-voltage (V) characteristic curve of graphene after STO growth shows that the electrical conductivity of the graphene was well preserved (see more details in Supplementary Information [SI. 1]).

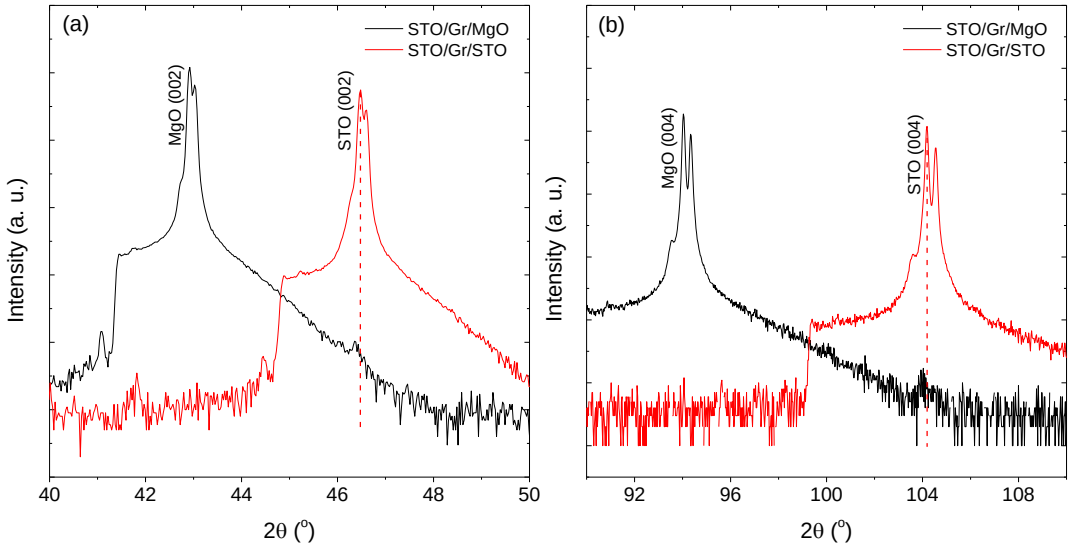

Figure 3: (a) XRD patterns of STO/Gr/MgO and STO/Gr/STO showing (002) peaks of MgO and STO; (b) XRD patterns of STO/Gr/MgO and STO/Gr/STO showing (004) peaks of MgO and STO. The slightly variance of STO peak positions between STO/Gr/STO and STO/Gr/MgO is the consequence of the systematic alignment error.

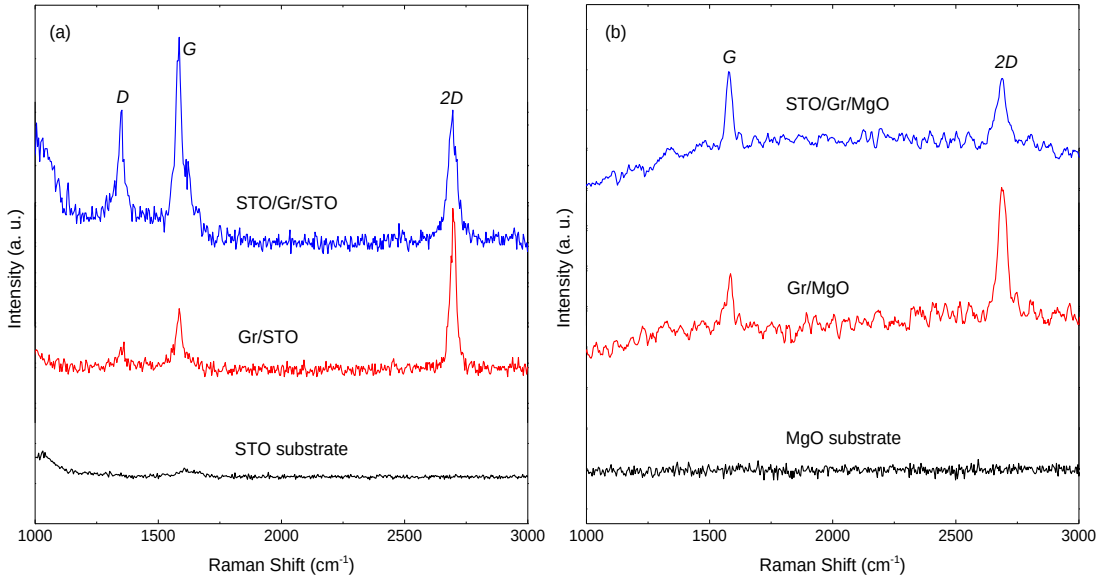

Figure 4: (a) Raman spectra of STO substrate, Gr/STO and STO/Gr/STO; (b) Raman spectra of MgO substrate, Gr/MgO and STO/Gr/MgO.

Raman spectroscopy of random regions on the samples was undertaken to confirm the presence of graphene after STO growth. The Raman spectrum of Gr/STO has three prominent peaks (*D, G* and *2D*) as shown in Fig. 4 (a). The *D* peak intensity (I_D) at ~1350 cm^{-1} is related to the amount of disorder in graphene layers.[23,24] The peak around 1580 cm^{-1}, denoted by *G*, is caused by the doubly degenerate zone centre photon E_{2g} mode.[25,26] The *2D* peak located at around 2690 cm^{-1}, is induced by a double resonance electron-phonon scattering process.[27] On Fig. 4 (b), it is noticeable that there are only two peaks (*G* peak and *2D* Peak) on the Raman spectrum of Gr/MgO. The absence of *D* peak reveals a higher crystalline quality of the graphene layer[27] in comparison with the graphene layer on STO. Notably, the ratios of *2D* peak intensities, I_{2D}/I_G, on Gr/STO and Gr/MgO are approximately 2, which are characteristic for monolayer graphene.

Raman spectra of STO/Gr/STO and STO/Gr/MgO samples are not very different from those of samples without STO thin films. No appreciable peak position shift is detected. But the full width at half maximum (FWHM) values of *2D* peaks increased after growing STO thin films on both Gr/STO and Gr/MgO samples. Besides, after the STO film deposition, the I_{2D}/I_G ratio decreases from nearly 2 to nearly 1 (STO/G/MgO sample) or even to less than 1 (STO/G/STO sample), see more details in Supplementary Information [SI. 2]. There are few reasons for such a decrease: the hole doping caused by the O_2 molecules[28,29,30,31], compressive strain in graphene[32,33], or multilayer graphene[25] formed after STO growth. The former

reason was ruled out as it is usually accompanied by substantial shift of *G* and *2D* peaks along with decrease of the full width at half maximum (FWHM) value of *G* peak,[28,34] (not observed in our samples). Thus, the decrease of I_{2D}/I_G ratio is attributed to the compressive strain in the graphene and formation of multilayer graphene caused by the construction of STO pillar structures on the defects.

Fig. 5 shows the high-resolution transmission electron microscopy (HRTEM) images of the STO/Gr/STO sample. It confirms that the STO film grown on Gr/STO highly ordered single crystal with an epitaxial matching with the substrate. Fig. 5 (a) and (b) illustrate the interfaces between the graphene and the STO layers. It is remarkable to observe the increase in the spacing between the STO cells (of the film and the substrate) and the sandwiched graphene layer (dark interfacial region in Fig. 5 (a)), as predicted from the modelling of the $STO_{film}/Gr/STO_{substrate}$ structure. The calculated geometry suggests that a distance about 0.3 nm is optimal. Also, there are well detected areas (Fig. 5(b)) without graphene layer, where the STO film grows epitaxially on the STO substrate. These areas serve as supportive pillars of the ordered single crystal STO film grown on the graphene layer. Observation of multilayer graphene, also shown in Fig. 5 (b), was an unexpected result because all samples were pre-screened (before STO deposition) to have single layer graphene. Nevertheless, the analysis of the interfacial intensity profile (the inset on the right hand side of Fig. 5 (b)), showed that the spacing between two brighter latitudinal lines is ~0.38 nm. This is consistent with the interlayer graphene distance. Further analysis of this interfacial

layer is provided in the Supplementary Information [SI. 3]. The partial folding of the single graphene layer is attributed to the shear strain introduced to the graphene layer due to the nucleation and growth of the STO pillars. The shear strain forces outplay the week interaction between the STO film, STO substrate and the sandwiched graphene layer, squeezing and folding the latter between two pillars. These results are in perfect agreement with the Raman spectroscopy analysis and the growth mechanism discussed above.

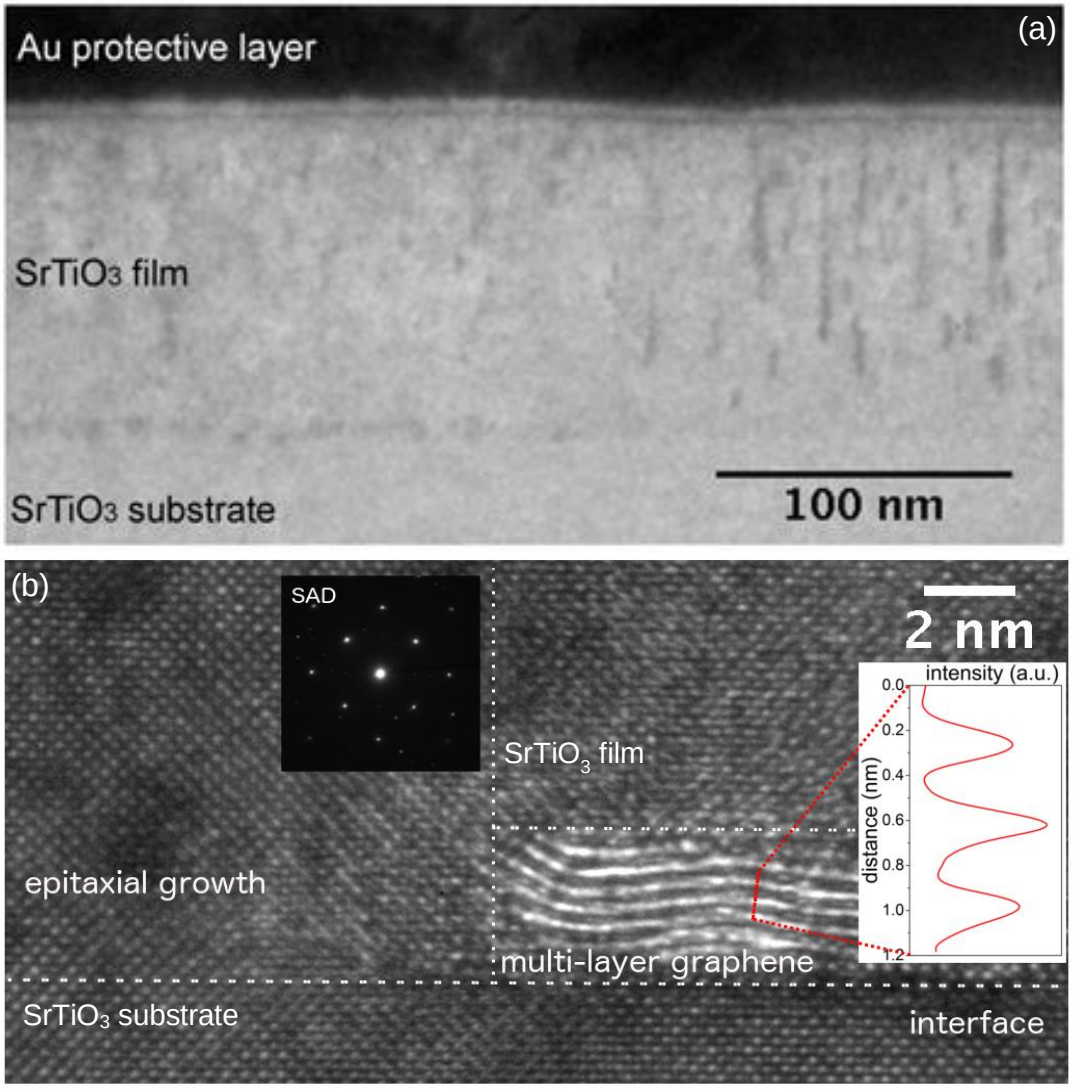

Figure 5: Cross-section TEM of the STO (100nm)/Gr/STO (001) thin film structure.

(a) low-magnification micrograph showing the film evolution; (b) a high resolution micrograph of interfaces: where interfacial layer (graphene) is not evidently visible on the left hand side of the image, and where a distinct interfacial layered structure is visible as bright contract (light element contrast) on the right hand side of the image; the inset on the left hand side shows selected area electron diffraction (SAED) pattern of the interface; the inset on the right hand side shows the spacing of layers at the interface is ~0.38 nm which is very close to graphite interlayer spacing of ~0.33nm[35].

In summary, the mechanism of the growth of epitaxial oxide (e.g. STO) thin films on graphene transferred onto STO and MgO substrates was revealed. The initial local defects in the graphene layer (e.g. grain boundaries) act like bridge-pillar spots that enable the epitaxial growth of STO thin film over the graphene layer. The growth of epitaxial STO pillar structures increases the interfacial sheer stress, which results in partial folding of the graphene layer. The results were confirmed by DFT modelling, HRTEM studies, XRD and Raman spectroscopy. The I-V measurement of the graphene after the STO film growth explicitly confirmed the conservation and the existence of the graphene layer after the deposition process. The evidence provided suggests that it is indeed possible to grow epitaxial oxide films on graphene.

Method

Single layer of graphene was grown on copper foils at temperatures up to 1000ºC by CVD. Before growth, the copper foils (25μm thickness) were pre-treated with acetic acid solution (50%) for 20 minutes and annealed at 1000 °C under 80 sccm H_2 gas for

10-60 minutes. The growth was conducted in a high temperature tube furnace by introducing 40 sccm of CH_4 gas at a total pressure of ~ 8 mbar for 10-30 minutes. Samples were unloaded from the quart tube after cooled to RT. Subsequently, a Poly(methyl methacrylate) (PMMA) layer was spin-coated on graphene to facilitate the transfer of graphene onto STO and MgO substrates. Then, the copper foils were etched. Finally, the PMMA/graphene layers were transferred onto STO and MgO substrates.

However, before transferring graphene onto STO substrate, the surface of STO substrate was thoroughly cleaned in ultrasonic bath using acetone, isopropanol, and deionized water, then dipped in buffered HF etchant. The etched STO substrates were annealed at 1000^{o}C for 1 hour before transfer. The treated surface of the STO substrate is believed to be atomically flat and dominated by TiO_2 termination.

After the graphene transfer, it is vital to eliminate the deleterious effects of the additional PMMA layer on top of the graphene layer. Therefore, as transferred samples were heated to 400^{o}C for 1 hour in ultrahigh vacuum (UHV) chamber to remove undesired PMMA and chemisorbed impurities, such as oxygen, carbon dioxide, carbon monoxide and water.

Gr/STO and Gr/MgO samples were annealed at 850^{o}C in vacuum before deposition. To prevent destruction of the graphene layer via thermal oxidation, STO thin films

(100nm) were grown on Gr/STO and Gr/MgO at 850°C by PLD in UHV (10^{-8} Torr) using a KrF excimer laser (λ=248 nm). A stoichiometric single phase STO target was ablated with a laser fluency of 2 J/cm^2 at 2 Hz. After deposition, as grown film was slowly cooled down to 600°C at a rate of 10°C/min in UHV and was subsequently *in-situ* post-annealed at 300 Torr O_2 pressure for 1 hour to compensate the potential oxygen loss during the growth.

The binding of the graphene sheet to the oxide has been calculated using density functional theory as implemented in the CRYSTAL14 software[36,37]. Full details of the all electron, local Gaussian basis set calculations are provided in Supplementary Information [SI. 4].

Raman spectroscopy was performed in air at RT on the STO and MgO substrates, Gr/STO and Gr/MgO substrates, and STO films grown on graphene of both substrates. The wavelength of excitation laser is 532 nm (2.33 eV in energy).

The surface of graphene was investigated with the aid of a high resolution field emission scanning electron microscope (FEG-SEM) LEO GEMINI 1525 FEG-SEM with an accelerating voltage of 5kV and working distance of ~6.5mm. Cross-sectional samples were prepared using an FEI Helios dual-beam and final thinning was done at 500eV with an Ar ion beam on a Fischione Nanomill. Transmission electron micrographs were taken using an aberration-corrected (at the image plane) FEI Titan

80-300 scanning/transmission electron microscope (S/TEM). All analysis was done with electron energy of 80 keV.

Acknowledgements

This work was partly funded from the UK Engineering and Physical Sciences Research Council (EPSRC) Grants EP/H012117/1 and EP/K016407/1; and the UK HPC Materials Chemistry Consortium (EPSRC Grant EP/F067496)

Author contributions

B.Z., C.W. and P.K.P. designed and conducted the STO film growth procedures; P.K.P., N.M.A. and N.K. conceived the project and designed the experimental set-up; N.M.H. performed modelling and theoretical calculation; C.W. carried out XRD characterisations; K.W. and O.S. grew and transferred graphene films; K.W. performed the Raman characterisations; B.Z., C.W. and K.W. analysed the XRD data and Raman data; B.Z. performed SEM experiments and analysed the data; V. T. carried out TEM experiments and data analysis; B.Z. and P.K.P. carried out the electrical measurements and analysed the data. All authors contributed to the data interpretation and manuscript preparation.

Competing financial interests

The authors declare no competing financial interests.

[1] Novoselov, K. S. et al. Electric Field Effect in Atomically Thin Carbon Films. *Science* **306,** 666-669 (2004).
[2] Novoselov, K. S. et al. Two-dimensional gas of massless Dirac fermions in graphene. *Nature* **438,** 197-200 (2005).
[3] Zhang, Y., Tan, Y. W., Stormer, H. L. & Kim, P., Experimental observation of the quantum Hall effect and Berry's phase in graphene. *Nature* **438,** 201-204 (2005).
[4] Geim, A. K. Graphene: status and prospects. *Science* **324,** 1530-1534 (2009).
[5] Novoselov, K. S. et al. A roadmap for graphene. *Nature* **490,** 192-200 (2012).
[6] Kim, K. S. et al. Large-scale pattern growth of graphene films for stretchable transparent elecrodes. *Nature* **457,** 706-710 (2009).
[7] Lee, C., Wei, X., Kysar, J. W. & Hone, J. Measurement of the elastic properties and intrinsic strength of monolayer graphene. *Science* **321,** 385-388 (2008).
[8] Novoselov, K. S. et al. Two-dimensional atomic crystals. *PNAS* **102[30],** 10451-10453 (2005).
[9] EI-Kady, M. F., Strong, V., Dubin, S. & Kaner, R. B. Laser Scribing of High-Performance and Flexible Graphene-Based Electrochemical Capacitors. *Science* **335,** 1326-1330 (2012).
[10] Saha, S. et al. Unconventional transport through graphene on $SrTiO_3$: A plausible effect of $SrTiO_3$ phase-transitions, *Scientific Reports* **4,** 6173-1~6 (2014).
[11] Yang, H. et al. Graphene barrister, a triode device with a gate-controlled schottky barrier, *Science* **336,** 1140-1143 (2012).
[12] Wang, X., Zhi, L. & Mullen, K. Transparent, conductive graphene electrodes for Dye-sensitized solar cell, *Nano Letters* **8[1],** 323-327 (2008).
[13] Miao, X. et al. High efficiency graphene solar cells by chemical doping, *Nano Lett.* **12[6],** 2745-2750 (2012).
[14] Yu, G. L. et al. Interaction phenomena in graphene seen through quantum capacitance, *PANS* **110[9],** 3282-3286 (2013).
[15] Lakin, K. M., Kline, G. R. & McCarron, K. T. High Q microwave acoustic resonators and filters, *IEEE Trans. Microwave Theory Tech.* **41[12],** 2139–2146 (1993).
[16] Ueda, M. et al. Development of an X-Band filter using air-gap-type film bulk acoustic resonators, *Japanese Journal of Applied Physics* **47[5],** 4007-4010 (2008).
[17] Hashimoto, K.-Y. RF bulk acoustic wave filters for communications. Norwood, MA, Artech House (2009). ISBN-13: 978-1-59693-321-7.
[18] Lee, B. et al. Conformal Al_2O_3 dielectric layer deposited by atomic layer deposition for graphene-based nanoelectronics. *Appl. Phys. Lett.* **92,** 203102-1~3 (2008).
[19] Zou, K., Hong, X., Keefer, D. & Zhu, J. Deposition of high-quality HfO_2on graphene and the effect of remote oxide phonon scattering. *Phy. Rev. Lett.* **105,** 126601-1~4 (2010).
[20] Wang, X., Tabakman, S. M. & Dai, H. Atomic layer deposition of metal oxides on pristine and functionalized graphene. *J. AM. Chem. Soc.* **130,** 8152-8153 (2008).
[21] Ni, Z. H. et al. Tunable stress and controlled thickness modification in graphene by annealing. *ACS Nano* **2[5],** 1033-1039 (2008).
[22] Momma, K. & Izumi, F. VESTA 3 for three-dimensional visualization of crystal, volumetric and morphology data. *J. Appl. Crystallogr.* **44,** 1272–1276 (2011).

[23] Ferrari, A. C. & Robertson, J. Raman spectroscopy of amorphous, nanostructured, diamond-like carbon, and nanodiamond. *Phil. Trans. R. Soc. Lond. A* **362,** 2477–2512 (2004).

[24] Casiraghi, C. et al. Raman spectroscopy of graphene edges. *Nano Letters* **9[4],** 1433-1441 (2009).

[25] Ferrari, A. C. et al. Raman spectrum of graphene and graphene layers. *Phys. Rev. Lett.* **97,** 187401-1~4 (2006).

[26] Ni, Z., Wang, Y., Yu, T. & Shen, Z. Raman spectroscopy and imaging of graphene. *Nano Res.* **1,** 273-291 (2008).

[27] Lee, D. S. et al. Raman sepctra of epitaxial graphene on SiC and of epitaxial graphene transferred to SiO_2. *Nano Letters* **8[12],** 4320-4325 (2008).

[28] Das, A. et al. Monitoring dopants by Raman scattering in an electrochemically top-gated graphene transistor. *Nature Nanotechnology* **3,** 210-215 (2008).

[29] Liu, L. et al. Graphene oxidation: thickness-dependent etching and strong chemical doping. *Nano Letters* **8[7],** 1965-1970 (2008).

[30] Ryu, S. et al. Atmospheric oxygen binding and hole doping in deformed graphene on SiO_2 substrate. *Nano Letters* **10,** 4944-4951 (2010).

[31] Hong, J. et al. Origin of new broad raman D and G peaks in annealed graphene. *Scientific Report* **3,** 2700-1~5 (2013).

[32] Lee, J. E., Ahn, G., Shim, J., Lee, Y. S. & Ryu, S. Optical separation of mechanical strain from charge doping in graphene. *Nature Communications* **3,** 1024-1~8 (2012).

[33] Yoon, D., Son, Y. W., & Cheong, H. Negative thermal expansion coefficient of graphene measured by Raman spectroscopy. *Nano Letters* **11,** 3227-3231 (2011).

[34] Pisana, S. et al. Breakdown of the adiabatic Born-oppenheimer approximation in graphene. *Nature Materials* **6,** 198-201 (2007).

[35] Casiraghi, C. et al. Rayleigh imaging of graphene and graphene layers. *Nano Letters* **7[9],** 2711-2717 (2007).

[36] Dovesi, R. et al. CRYSTAL14 User's Manual (University of Torino, Torino, 2014).

[37] Dovesi, R. et al. *Int. J. Quantum Chem.* **114**, 1287 (2014).

Supplementary information

Growth of Epitaxial Oxide Thin Films on Graphene

Bin Zou[1], Clementine Walker[1], Kai Wang[1], Vasiliki Tileli[1], Olena Shaforost[1], Nicholas M. Harrison[2], Norbert Klein[1], Neil M. Alford[1] and Peter K. Petrov[1*]

[1] *Department of Materials, Imperial College London, Prince Consort Road, London, SW7 2AZ, UK*

[2] *Department of Chemistry, Imperial College London, Imperial College Road, London, SW7 2AZ, UK*

Supplementary information

SI. 1. Current (I)-Voltage (V) characteristic of graphene layer on $SrTiO_3$/Graphene/$SrTiO_3$ (STO/Gr/STO) sample

Electrodes (50nm Au/4nm Ti) were deposited on graphene using a Mantis DC magnetron sputtering system. The on-wafer electrical measurements were carried out on a Signatone probe-station. Four probe measurements (I-V characteristics) were carried out using an Agilent B1500A semiconductor device analyser. All electrical measurements were performed at room temperature and atmosphere pressure unless otherwise indicated.

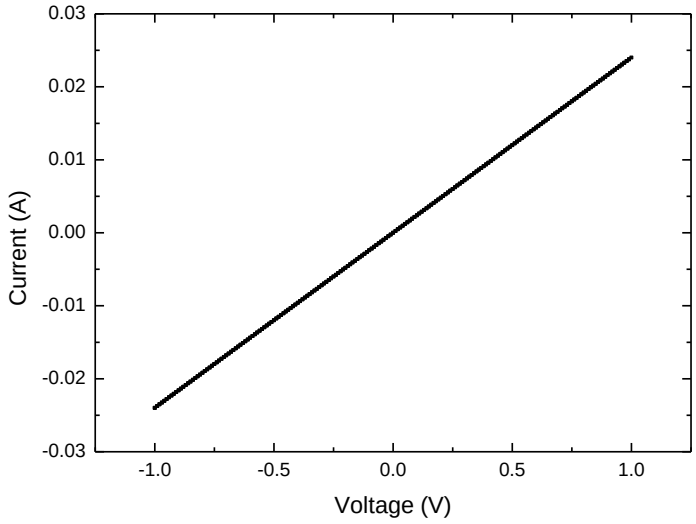

Figure S1: I-V curve measured on graphene after STO growth

Fig. S1 shows I-V curve that was measured on Au/graphene of two corners across sample after STO growth. The estimated graphene resistivity was below ~100 μΩ·cm, which is not very far away from the values measured for conventional graphene layers. Nevertheless, this is a clear indication that the graphene layer is still conductive after the STO thin film deposition using PLD.

SI. 2. Analysis of Raman spectra

Table S1. Raman peak properties

Samples	Peaks	Peak position (cm^{-1})	FWHM (cm^{-1})	Intensity	Ratios
Gr/STO	D	1351	28	33	I_D/I_G=0.56
	G	1585	30	59	

	2D	2698	27	126	I_{2D}/I_G=2.14
STO/Gr/STO	D	1349	30	61	I_D/I_G=0.64
	G	1585	37	95	
	2D	2695	41	61	I_{2D}/I_G=0.64
Gr/MgO	G	1585	16	17	
	2D	2690	34	35	I_{2D}/I_G=2.01
STO/Gr/MgO	G	1585	22	76	
	2D	2690	44	76	I_{2D}/I_G=1

Fig. S2 shows Raman spectrum of STO/Gr/MgO sample, while the Fig. S3, illustrates the Raman mapping data of the STO/Graphene/MgO structure. The colour brightness in Fig. S3 corresponds to the peak intensity of respective peak. Even though there are discernible areas showing no graphene (dark colour), the graphene *G* band and *2D* band can be detected over the whole mapping area, confirming that graphene was not destroyed by the deposition process.

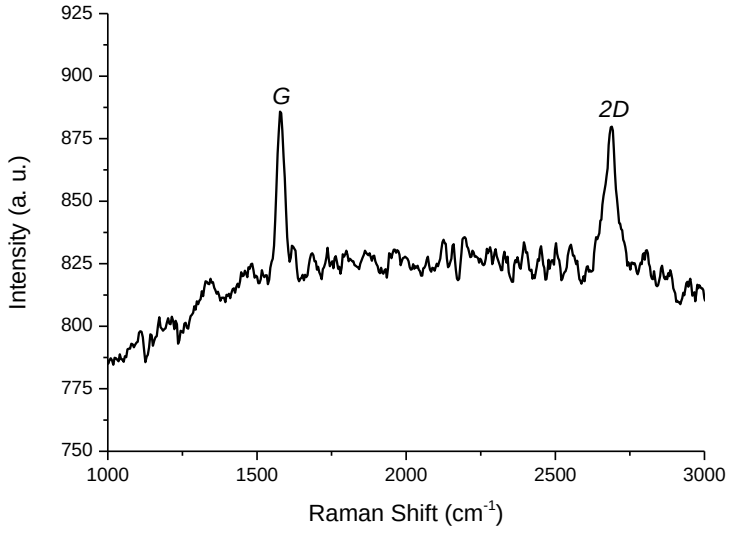

Figure S2: Raman spectrum of STO/Gr/MgO

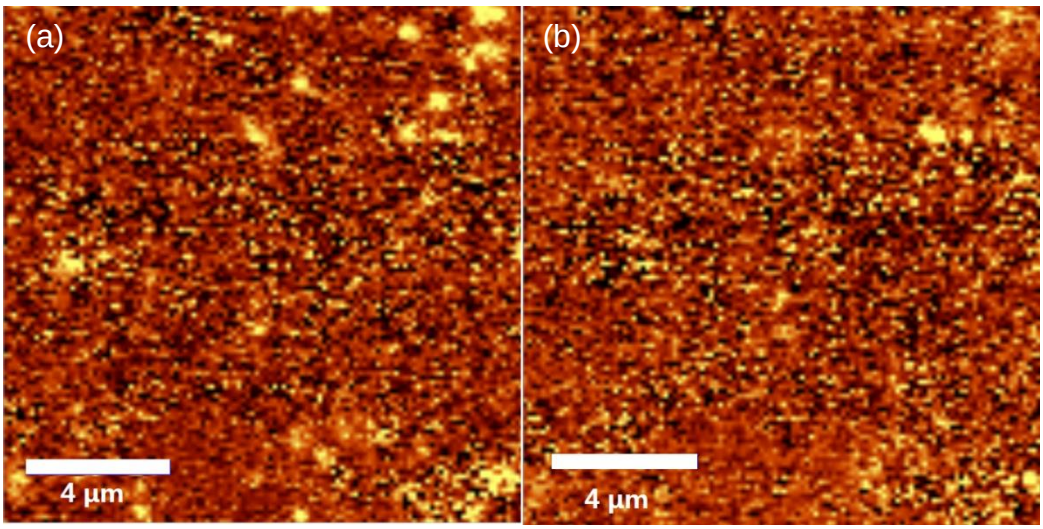

Figure S3: Raman mappings of STO/Gr/MgO: (a) G band and (b) 2D band

SI. 3. Chemical evaluation of the Gr/STO interface on STO/Gr/STO sample

The chemical evaluation of the Gr/STO interface was performed on an aberration-corrected (at the image plane) FEI Titan 80-300 scanning/transmission electron microscope (S/TEM) in STEM mode using a Gatan Tridiem electron energy-loss spectrometer (EELS) with an energy resolution of 0.7eV.

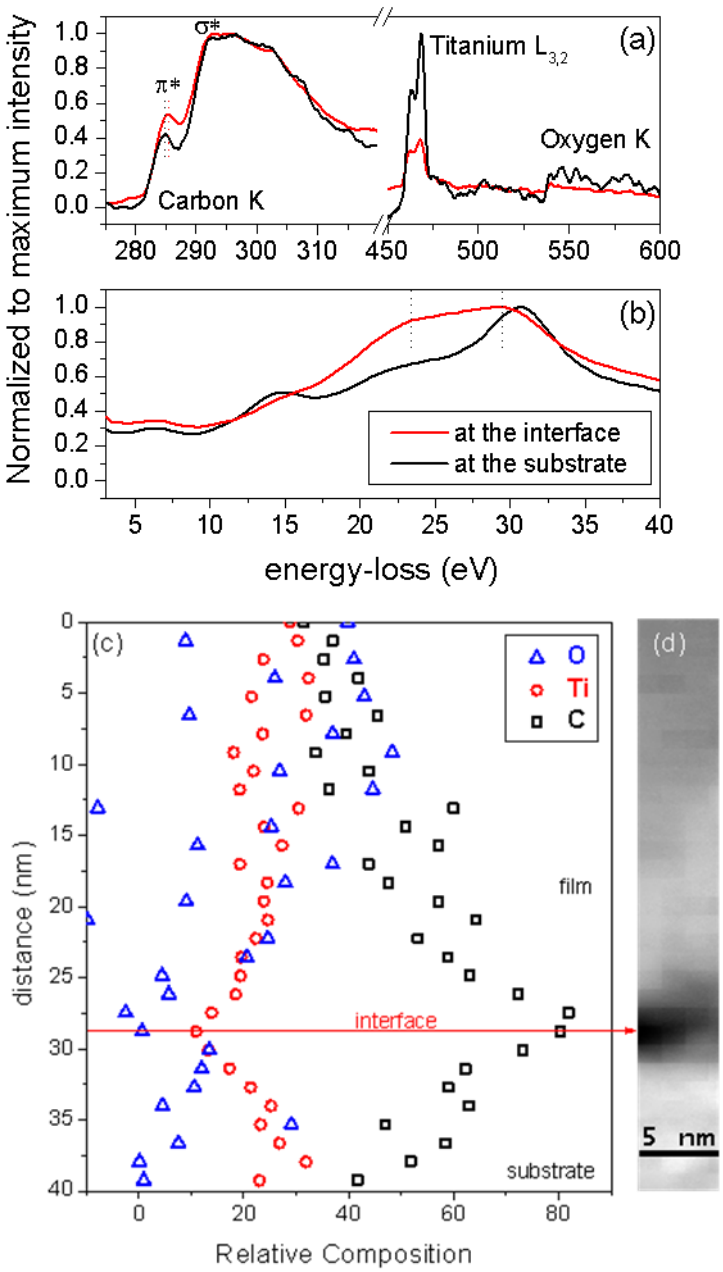

Figure S4: Energy electron-loss spectra acquired at the interface and on the STO substrate in (a) the core-loss region detailing the Carbon K, the Titanium $L_{3,2}$ and the Oxygen K edges; and (b) in the low-loss region monitoring the plasmon loses; (c) quantitative analysis of the spectrum image; (d) taken along the thin film structure reveals high carbon content at the interface associate with an overall reduction both in Ti and O relative composition.

To evaluate the chemical character of the carbon-based interface, electron energy-loss spectra were acquired extending from the substrate to the interface. Fig. S4(a) depicts the core-loss excitations of the C K, Ti $L_{3,2}$, and O K edges, which represent the local density of states of the material. The first C peak corresponds to the π^* transition and the shift to higher energy of the spectrum at the interface (285.4eV) compared to the substrate one (284.8eV) confirms the graphene-nature of the interface.[1] The σ^* transition of the interface is highly reduced and this could be attributed to partly oxidized structure. Indeed, inspection of the plasmon loss region at the interface, Fig. S4(b), reveals two peaks at 23.5 eV and 29.5 eV, which correspond to graphene oxide and graphene respectively. Furthermore, quantitative analysis of the spectrum image shown in Fig. S4(c) reveals that the relative amount of both Ti and O is highly reduced at the interface followed by an increase in C content. This can be visually and intuitively observed by the dark colour at interface in Fig. S4(d). It is noted that the cross-sectional TEM sample preparation process always results in carbonaceous amorphization of the sides of the lamellae. However, the results suggest that the crystalline nature of the graphene interfacial layer is preserved.

SI. 4. Density functional theory (DFT) modelling

All electron, local atom centred Gaussian basis set, calculations were performed using the CRYSTAL14 software[2,3]. The basis sets for STO were adapted for use in condensed systems and of triple valence quality (ie: three independent radial functions for each valence electron) with polarisation functions. These basis sets have been described and used in previous studies of SrO[4] and TiO_2[5,6]. For the graphene sheet a modified 631G* basis set was used.[7] Electronic exchange and correlation were

described within density functional theory in the B3LYP approximation which has been used extensively in previous studies of titanates[5,6] and graphene derived nanostructures[7]. Long range London dispersion interactions were included through the empirical correction scheme proposed by Grimme[8]. For the C and O centres the atomic radius (Angstrom) and C_6 coefficient (Jnm^6mol^{-1}) were set to (1.452, 1.75) and (1.342, 0.70) respectively and the overall scaling (s6) set to 1.05 which are the default values in the CRYSTAL14 code[2,3].

$SrTiO_3$ was described in the cubic perovskite structure with lattice constant 3.898 Å and the graphene sheet with lattice constant 2.46 Å. The graphene STO (100) interface was modelled in a 2D-periodic square cell of side 8.85 Å containing 10 $SrTiO_3$ formula units representing four atomic layers of the (100) surface in a $\begin{pmatrix} 2 & 1 \\ -1 & 2 \end{pmatrix}$ supercell of its primitive surface unit cell (of dimensions 8.72 Å×8.72 Å) and 60 carbon atoms representing graphene sheets at both the SrO and TiO_2 terminations in a $\begin{pmatrix} 1 & 4 \\ 4 & 1 \end{pmatrix}$ supercell of the primitive graphene unit cell (with lattice vectors of length 8.87 Å at an angle of 87.8 degrees). A reciprocal space sampling on a Pack-Monkhurst grid of shrinking factor 2, which results in 3 irreducible k-points in the first Brillouin zone, was adopted as it is sufficient to define the total energy to within 10^{-4} eV per cell. Structural optimization of internal coordinates only was performed by relaxing all atoms of the slab model, using the Broyden-Fletcher-Goldfarb-Shanno scheme, as implemented in CRYSTAL14[2]. The thresholds for the maximum and the rms forces (the maximum and the rms atomic displacements) were set to 0.00045 and 0.00030 (0.00180 and 0.0012) in atomic units. Geometry optimization was terminated when all four conditions were satisfied simultaneously. The corrugation potential, for sliding the

graphene sheet across the STO(100) surface, was computed by offsetting the origin of the sheet relative to the underlying surface and then relaxing the atoms at the oxide surface and in the graphene sheet only along the direction perpendicular to the surface. This was performed on a 10×10 grid of offsets exploring the area of the surface supercell.

References

[1] Mkhoyan, K. A. et al. Atomic and electronic structure of graphene-oxide. *Nano Letters* **9[3],** 1058-1063 (2009).

[2] Dovesi, R. et al. CRYSTAL14 User's Manual (University of Torino, Torino, 2014).

[3] Dovesi, R. et al. *Int. J. Quantum Chem.* **114,** 1287 (2014).

[4] Erba, A., El-Kelany, Kh. E., Ferrero, M., Baraille, I. & Rérat, M. Piezoelectricity of $SrTiO_3$: An Ab initio Investigation. *Phys. Rev. B* **88,** 035102 (2013).

[5] Dubrovinsky, L. S. et al. Materials Science - The Hardest Known Oxide. *Nature* **410,** 653-654 (2001).

[6] Lindsay, R. et al. Revisiting the Surface Structure of TiO_2 (110): A Quantitative low-Energy Electron Diffraction Study. *Phys. Rev. Lett.*, **94[24],** 246102 (2005).

[7] Warner, J. H. et al. Structural Transformations in Graphene Studied with High Spatial and Temporal Resolution. *Nature Nanotechnology* **4[8],** 500–504 (2009).

[8] Grimme, S. Density functional theory with London dispersion corrections. *WIREs Comput. Mol. Sci.* **1[2],** 211-228 (2011).